Supplementary Materials for

Agent-based modeling of stress anisotropy driven nematic ordering in growing biofilms

Changhao Li[1], Japinder Nijjer[4], Luyi Feng[1], Qiuting Zhang[4], Jing Yan[4,5,*], Sulin Zhang[1,2,3*]

*Corresponding author. Email: suz10@psu.edu or jing.yan@yale.edu

[1]Department of Engineering Science and Mechanics, Pennsylvania State University, University Park, PA, USA.

[2]Department of Biomedical Engineering, Pennsylvania State University, University Park, PA, USA.

[3]Department of Material Science and Engineering, Pennsylvania State University, University Park, PA, USA.

[4]Department of Molecular, Cellular and Developmental Biology, Yale University, New Haven, CT

[5]Quantitative Biology Institute, Yale University, New Haven, CT

Supplementary Text

Agent-based model (ABM)

Our agent-based model is built on the previous models developed by Beroz et al. (1) and others (2, 3), and has successfully applied to the differential growth and self-patterning problem of *V. cholorae* biofilms (4). As shown in **Fig. S1**, cells in the biofilm are modeled as elongating and dividing spherocylindrical agents and the surrounding hydrogel is modeled as a collection of spherical agents. We adopt the Hertzian and JKR contact models to address the nonlinear elastic deformation and the interfacial adhesions in the biofilm-hydrogel system. The details of agent particle geometries, interactions, governing equations, and parameter settings are introduced below.

Single cell geometry

For simplicity, we assume that a single spherocylinder represents the space occupied by the combination of a single cell and its surrounding extracellular matrix. The shape of spherocylinders

can be determined by their length L and radius R, with the volume $V = \frac{4}{3}\pi R^3 + \pi R^2 L$. For a single cell, we assume the growing speed of cell length $\frac{dL}{dt}$ is a constant, and the radius R keeps the same, leading to an exponential volume growth law $\frac{dV}{dt} = \gamma V$. To introduce randomness into the model, we assume the growth rate γ follows the normal distribution $\gamma \sim N(\gamma_0, 0.2\gamma_0)$, where γ_0 is the average growth rate calibrated from experiments. In simulations, the continuous exponential growth is implemented as a sequence of discrete length increments of $\Delta L = \gamma\left(\frac{4}{3}R + L\right)\Delta t$, where Δt is the length of timesteps.

We model the cell division as the following: when the length of a mother cell reaches the division length L_{max}, it is instantaneously replaced by two equal-sized daughter cells with the initial length $L_0 = \frac{L_{max}}{2} - R$. As shown in **Fig. S1**, L_0 is determined by the criteria where two daughter cells have the same total head-to-tail length ($L + 2R$) as the mother cell. Then it follows, for a cell with the initial length L_0 and the growth rate γ, the cellular doubling time is $t_{double} = \frac{1}{\gamma}\log\left(\frac{10R + 6L_0}{4R + 3L_0}\right)$. In simulations, the division is implemented as the following: in a single timestep, if the length of a mother cell reaches L_{max}, the length of this cell is altered to L_0, as the first daughter cell. The second daughter cell is generated by directly copying the first, then their center positions are changed so that they occupy the same head-to-tail position as the mother cell without overlapping.

It should be noted that, we use a hard-core, soft-shell model to capture the mechanical properties of the cell-matrix composite. We assume the spherocylindrical region of a single cell can be divided into two regions with different contact stiffnesses E. The outer region represents the soft extracellular matrix ($E_{mat} \sim 300\ Pa$) (5), and the inner region represents the rigid bacteria cell ($E_{cell} \sim 50\ kPa$) (6). We denote the radius of the rigid cell (inner region) by R_c to differentiate it

with the radius of cell-matrix composite R, and all the word "cell" represents "cell-matrix composite" in the following descriptions, unless any special declaration.

Cell-cell repulsion

For cell-cell interactions, we neglect any adhesion and friction between cells, but only consider their elastic contact. We apply the linear elastic Hertzian contact theory (7) to quantify the repulsive contact forces on cell i by cell j, written as

$$F_{cell-cell,ij} = \begin{cases} -\frac{5}{2}E_0 R^{1/2}\delta_{ij}^{3/2}\hat{e}_{ij}, \delta_{ij} < R - R_c \\ -\frac{5}{2}(E_0 R^{1/2}(R-R_c)^{3/2} + E_c R^{1/2}(\delta_{ij} - R + R_c)^{3/2})\hat{e}_{ij}, \delta_{ij} > R - R_c \end{cases}, \quad \textbf{(1)}$$

where E_0 and E_c denote the effective contact stiffnesses of the extracellular matrix and rigid cells respectively, R_c is the radius of the center rigid cell, δ_{ij} is the overlapping distance, and $\hat{e}_{ij}$ denotes the unit vector normalized from the distance vector d, defined as the smallest distance between two cell centerlines. The overlapping distance δ_{ij} is given by $\delta_{ij} = 2R - |d|$. Note that, we generalize all the contact forces (including point-point contact and line contact) by the scaling relation $F \sim \frac{5}{2}E_0 R^{1/2}\delta^{3/2}$, to avoid the computational step to decide if two cylinders are perfectly parallel with each other. Strictly, for the perfectly parallel contact case, the scaling of the contact forces should have been $F \sim \frac{\pi}{4}E_0 m\delta$, where m is the contact length. We validate this simplification by comparing the above two scaling relations (**Fig. S3A**), where we set the contact length $m = 1.6\,\mu m$ (the average cell length) and the contact radius $R = 0.8\,\mu m$ (the cell radius in our model), and the difference of contact forces is negligible. We also show that the above simplification has trivial effects on cell alignment and stress distributions. As shown in **Fig. S3B**, we compare two biofilms under different treatments of the cell-cell contact (the left is the simplified contact model used throughout our work, and the right is the modified version by considering the perfect parallel contact), and find that the spreading radius of biofilm, the cell alignments, and the onset threshold of verticalization are nearly identical between two simulations. Furthermore, we compare the spatiotemporal evolution of the hydrostatic pressure and the equivalent shear stress between the simplified and the modified contact model (**Fig. S3C**). The

modified contact interaction does not significantly alter the time evolution of average stresses, stress spatial distribution, and the cell orientational order.

Correspondingly, the moment of contact force $F_{cell-cell,ij}$ about cell center is given by

$$M_{cell-cell,ij} = s_r \hat{n}_i \times F_{cell-cell,ij}, \quad \textbf{(2)}$$

where $\hat{n}_i$ is the unit vector denoting cell orientation (from cell center to the contact point) and s_r is the parametric coordinate of the contact point along the center line of the cell.

Cell-gel interactions

On the interface between the biofilm and the surrounding hydrogel, we apply a JKR-type model to capture the elastic contact and the adhesion between a cell agent i and a coarse-grained gel particle j. For the elastic contact, we use a similar linear elastic Hertzian contact interaction with Eq. **(1)**, written as

$$F_{cell-gel,ij}^{rep} = \begin{cases} -\frac{5}{2}E_0 {R_{eq}}^{1/2} \delta_{ij}^{3/2} \hat{e}_{ij}, \delta_{ij} < R - R_c \\ -\frac{5}{2}(E_0 {R_{eq}}^{1/2}(R-R_c)^{3/2} + E_c {R_{eq}}^{1/2}(\delta_{ij} - R + R_c)^{3/2})\hat{e}_{ij}, \delta_{ij} > R - R_c \end{cases}, \quad \textbf{(3)}$$

where $R_{eq} = \frac{2R_{gel}R}{R + R_{gel}}$ is the equivalent radius of contact, R_{gel} is the radius of coarse-grained gel particles, and the overlapping distance $\delta_{ij} = R + R_{gel} - |d|$ is determined by a similar method considering the minimal distance between the center of the gel particle to the cell center line.

We assume cell-gel adhesion forces are proportional to $\gamma_{cell-gel}$, which is the energy release per unit area given by $\gamma_{cell-gel} = \gamma_{cell} + \gamma_{gel} - \gamma^*$, the surface energy of cell and gel minus the interfacial energy γ^*. Naturally, cell-gel adhesion forces are also proportional to the contact area, which gives

$$F_{cell-gel,ij}^{adh} = \pi a^2 \gamma_{cell-gel} \hat{e}_{ij}, \quad \textbf{(4)}$$

where a is the equivalent radius of contact area, given by the simplified geometric relation $a = \sqrt{\delta_{ij} R_{eq}}$. For simplicity, our model neglects the cohesion-decohesion asymmetric behavior in the original JKR model, as the decohesion behavior rarely happens on the continuously expanding biofilm-gel interface.

Similarly, the moment about the cell center, for the repulsive cell-gel contact force $F_{cell-gel,ij}^{rep}$ and the cell-gel adhesion $F_{cell-gel,ij}^{adh}$, can be given by

$$M_{cell-gel,ij}^{rep} = s_r \hat{n}_i \times F_{cell-gel,ij}^{rep}, \quad \textbf{(5)}$$

and

$$M_{cell-gel,ij}^{adh} = s_r \hat{n}_i \times F_{cell-gel,ij}^{adh}. \quad \textbf{(6)}$$

Gel-gel interactions

We treat the surrounding agarose gel as a soft viscoelastic material, using the coarse-grained modeling approach to address its mechanical behavior. The basic elements of the coarse-grained model are spherical particles of radius R_{gel} with harmonic interactions. We set the pairwise interaction energy between the gel particles as $E_{gel,2} = \Sigma_{ij} \frac{k_r}{2} (\xi_{ij} - \xi_0)^2$,with the cut-off radius $R_{gel,2}^{c}$, where ξ_{ij} is the distance between particle i and j, ξ_0 is the equilibrium distance, and k_r is the spring constant. To capture the gel shear modulus, we also introduce a three-body interaction energy where $E_{gel,3} = \Sigma_{ijk} \frac{k_\zeta}{2} (\zeta_{ijk} - \zeta_0)^2$, with the cut-off radius $R_{gel,3}^{c}$, where ζ_{ijk} is the bond angle formed by particle i, j, and k. We also considered the normalized Stokes viscosity of gel particles to address the viscoelasticity behavior also stabilize the gel system, given by $F_{stokes,i} = -\eta_{gel} u_i$, where η_{gel} is the normalized viscosity coefficient and u_i is the velocity vector of the gel particle i.

Cell-to-substrate interactions

Considering the glass substrate in experiments has significantly larger Young's modulus compared with cells and gel, we model the substrate as a rigid, two-dimensional infinite plane located at $z = 0$. Similarly, we apply the linear elastic Hertzian contact model to represent the repulsion between cells and the substrate. On the other hand, we assume the cell-substrate adhesion is related to the equivalent contact area between cells and the substrate, by the Derjaguin approximation (8).

For the cell-substrate repulsive contact, we use a generalized Hertzian contact formula to account for the cell orientation-dependent contact energy. Similar to Eq. (1) and (2), the elastic contact energy is given by $E_{el,i} = E_0 R^{1/2} \delta_i^{5/2}$, where δ_i is the equivalent penetration depth which depends on the average penetration depth and the cell-substrate relative angle, given by the explicit formula:

$$\delta_i^{5/2} = \int_{-L/2}^{L/2} \left[R^{1/2} \left| \hat{n}_{\parallel,i} \right|^2 \delta^2(s) + \frac{4}{3} \left(1 - \left| \hat{n}_{\parallel,i} \right|^2 \right) \delta^{3/2}(s) \right] ds, \quad \textbf{(7)}$$

where $\hat{n}_{\parallel,i}$ is the normalized projection of the ith cell director on the substrate ($z = 0$). The overlap function $\delta(s)$ denotes the overlapping distance between the cell and the substrate at the local cell-body coordinate $-L/2 \le s \le L/2$. Then, the net force $F_{el,i}$ and moment $M_{el,i}$ from the cell-substrate elastic repulsion can be given by

$$F_{el,i} = 2E_0 R^{1/2} \int_{L/2}^{-L/2} \hat{z} \left[R^{1/2} \left| \hat{n}_{\parallel,i} \right|^2 \delta(s) + \left(1 - \left| \hat{n}_{\parallel,i} \right|^2 \right) \delta^{1/2}(s) \right] ds, \quad \textbf{(8)}$$

$$M_{el,i} = 2E_0 R^{1/2} \int_{L/2}^{-L/2} \left[s\hat{n}_i \times \hat{z} \right] \left[R^{1/2} \left| \hat{n}_{\parallel,i} \right|^2 \delta(s) + \left(1 - \left| \hat{n}_{\parallel,i} \right|^2 \right) \delta^{1/2}(s) \right] ds, \quad \textbf{(9)}$$

where $\hat{z}$ is the unit vector perpendicular to the substrate.

Similar to Eq. (4), we assume the cell-substrate adhesion energy by the form of $E_{ad,i} = -\Sigma_0 A_i$, where Σ_0 is the adhesion energy density and A_i is the equivalent contact area between cell i and the substrate. The equivalent contact area is given by

$$A_i = \int_{-L/2}^{L/2} a(s)ds = \int_{-L/2}^{L/2} \left[R^{1/2}\left|\hat{n}_{\parallel,i}\right|^2 \delta^{1/2}(s) + \pi R\left(1 - \left|\hat{n}_{\parallel,i}\right|^2\right) H(\delta(s))\right] ds, \quad \textbf{(10)}$$

where $H(\cdot)$ is the Heaviside step function. Thus, the net adhesive force $F_{ad,i}$ and moment $M_{ad,i}$ are:

$$F_{ad,i} = -\Sigma_0 \int_{-L/2}^{L/2} \hat{z}\left[\frac{1}{2}R^{1/2}\left|\hat{n}_{\parallel,i}\right|^2 \delta^{-1/2}(s)\right] ds - \hat{z}\Sigma_0 \pi R\left(1 - \left|\hat{n}_{\parallel,i}\right|^2\right), \quad \textbf{(11)}$$

$$M_{ad,i} = -\Sigma_0 \int_{-L/2}^{L/2} \left[s\hat{n}_i \times \hat{z}\right]\left[\frac{1}{2}R^{1/2}\left|\hat{n}_{\parallel,i}\right|^2 \delta^{-1/2}(s)\right] ds - \left[s_0\hat{n} \times \hat{z}\right]\Sigma_0 \pi R\left(1 - \left|\hat{n}_{\parallel,i}\right.\right. \quad \textbf{(12)}$$

where s_0 denotes the cell-body coordinate such that $\delta(s_0) = 0$. Namely, the condition $\delta(s_0) = 0$ gives the point where a cell detaches from the substrate.

Viscosity of cells

We consider two sources of viscosity of cells: a bulk viscous force due to the friction from extracellular matrix environment and a surface viscous force due to the substrate. The environmental viscous force and moment are given by Stokes' law,

$$F_{stokes,i} = -\eta_0 u_i, \quad \textbf{(13)}$$

$$M_{stokes,i} = -\eta_0 \int_{L/2}^{L/2} s\hat{n}_i \times \left(\omega_i \times s\hat{n}_i\right) ds = -\frac{\eta_0}{12}\omega_i L^3, \quad \textbf{(14)}$$

where η_0 is the normalized environmental viscosity, u_i is the velocity of the center of mass, and ω_i is the angular velocity. The substrate viscous force and moment are taken to be of the form

$$F_{surface,i} = -\int_{-L/2}^{L/2} \frac{\eta_1 a(s)}{R}\left[u_i(s) - \left(u_i(s)\cdot\hat{z}\right)\hat{z}\right] ds, \quad \textbf{(15)}$$

$$M_{surface,i} = -\int_{-L/2}^{L/2} \frac{\eta_1 a(s)}{R} s\hat{n}_i \times \left[u_i(s) - \left(u_i(s)\cdot\hat{z}\right)\hat{z}\right] ds, \quad \textbf{(16)}$$

where η_1 is the viscous coefficient along the substrate.

Interactions between the gel particles and the substrate

We use two types of interactions to mimic the experimental condition where the gel is adhered to the substrate. The first type of interaction is gel-substrate elastic contacts. Here we again apply the linear elastic Hertzian contact theory between a sphere and a flat rigid surface, and the elastic contact energy is given by $E_{gel-surface,i} = E_1 R_{gel}^{1/2} \delta_i^{5/2}$, where E_1 is the contact stiffness between gel particles and the substrate and δ_i is the overlap between the gel particle and the substrate. The second type is the gel-substrate adhesion, serving as the energy barrier for the experimentally observed delamination on the gel-substrate interfaces. Similarly, we take the adhesion energy as $E_{ad,gel,i} = -\Sigma_1 A_{gel,i}$, where Σ_1 is the adhesion energy density and the equivalent contact area is given by $A_{gel,i} = \pi R_{gel} \delta_i$.

Equations of motion

The equations of motion for *V. cholorae* cells (spherocylinders) are given by Newton's rigid body dynamics:

$$\begin{pmatrix} F_{net,i} \\ M_{net,i} \end{pmatrix} = \begin{bmatrix} m & 0 \\ 0 & I_i \end{bmatrix} \begin{pmatrix} \dot{u}_i \\ \dot{\omega}_i \end{pmatrix} + \begin{pmatrix} 0 \\ \omega_i \times I_i \omega_i \end{pmatrix}, \quad \textbf{(17)}$$

where $F_{net,i}$ and $M_{net,i}$ are the total force and moment vector, and I is the moment of inertia. All the variables are expressed in the body-fixed coordinate system, then transformed into the global coordinate system. We add a small random noise to the net force and moment vectors of the cells at every timestep ($10^{-7}E_0R^2$ for forces and $10^{-7}E_0R^3$ for moments), to represent the environmental fluctuations required for breaking the symmetry.

For the equations of motion of hydrogel particles (spheres), we neglect the rotational degrees of freedom of hydrogel agents, because it is not physical to consider the particle spin when modeling the elastic behavior of hydrogels. Essentially, hydrogel is modeled as a collection of mass points (with a spherical shape) connected by springs. Therefore, the equations of motion are given by Newton's second law $F_{tot,i} = m\dot{u}_i$, where $F_{tot,i}$ is the net force and $\dot{u}_i$ is the acceleration. To prepare the initial amorphous stress-free geometry, we begin with a body-centered cubic crystalline geometry with lattice parameter a, where $a = 1.15\,R_{gel}$. Subsequently, we assigned the system with an initial temperature of $300\,K$ and annealed it (using NVT thermostat) until it reached a final configuration that is amorphous and stress-free (spatial averaged residual pressure smaller than 0.01 kPa).

Choice of parameters

The cell radius R and the division (maximum) length L_{max}: we set $R = 0.8\,\mu m$ and $L_{max} = 3.6\,\mu m$ to match the experimentally measured mean radius and division length.

The hard-core stiffness E_c, hard-core radius R_c, and soft-shell stiffness E_0: we set hard-core stiffness $E_c = 30\,kPa$ to match the reported experimental measurement (8 to 47 kPa) (6), while the soft-shell stiffness $E_0 = 300\,Pa$ according to the previous rheology experiments (1). We set the hard-core radius as $R_c = 0.5\,\mu m$.

viscosity coefficients η_0, η_1, η_{gel}: We take $\eta_0 = 2 \times 10^{-6}\,Pa \cdot s \cdot m$, and $\eta_1 = 2 \times 10^{5}\ Pa \cdot s$ to match the previous rheology experiments. Taken the water viscosity $\mu_W = 8.9 \times 10^{-4}\,Pa \cdot s$,

η_{gel} is calculated as $\eta_{gel} = 6\pi\mu_W R_{gel} \approx 2 \times 10^{-8}\, Pa \cdot s \cdot m$. Interestingly, we found η_1 and the gel stiffness jointly control the biofilm morphology, reported in the reference (9).

The spring constant k_r and equilibrium length ξ_0: The Young's modulus of the agent-based gel system is given by (10) $Y = \frac{1}{V}\frac{\partial^2(E_{gel,2} + E_{gel,3})}{\partial\epsilon^2} \simeq \frac{k_r}{2\xi_0}$, under the condition $k_\zeta \ll k_r$. Generally, a smaller ξ_0 leads to a denser gel system and better approximation to a continuum solid. Here we choose $\xi_0 = 0.6\ \mu m$ as a result of a trade-off between simulation quality and computational cost, as the simulation time is proportional to $\frac{1}{\xi_0^3}$. k_r ranges from $1.2 \times 10^{-4}\, Nm^{-1}$ to $1.2 \times 10^{-1}\, Nm^{-1}$ corresponding to the Young's modulus $Y = 0.1\ kPa$ to $Y = 100\ kPa$.

Radius of agent gel particle R_{gel}: in order to mimic the continuum constraints posed by the hydrogel in the experiment, R_{gel} should be larger than ξ_0. On the other hand, R_{gel} cannot be significantly larger than the cell radius R, as this will introduce unphysical contacts at the biofilm-gel interface. Taking both requirements into consideration, we choose $R_{gel} = 1.0\ \mu m$, which is nearly double the equilibrium distance $\xi_0 = 0.6\ \mu m$ and we keep $R_{gel} \approx R$.

Gel-substrate contact stiffness E_1 and adhesion energy density Σ_1: we choose $E_1 = 5\ kPa$ and $\Sigma_1 = 5 \times 10^{-2}\, N \cdot m^{-1}$ for all gel stiffnesses.

Simulation settings and boundary conditions

In simulations for both G-I and G-II biofilms, the surrounding hydrogel is modeled as a homogeneous, isotropic and linear elastic material using the agent-based model elaborated above. For the G-II biofilm, we set the simulation domain as the cubic box with the size of $200 \times 200 \times 120\ \mu m^3$, where the initial geometry is initialized with a single cell lying parallel to the substrate without initial velocity and acceleration, surrounded by gel particles filling the entire

simulation domain. A small hemisphere around the seed cell is vacated to avoid initial overlap between cell and hydrogel particles. For the G-I biofilms, the simulation domain size is $200 \times 200 \times 200\ \mu m^3$ due to the removal of the rigid substrate. Similarly, the initial seed cell is placed in the center of the cubic box, with a small spherical region vacated. For both kind of simulations, we fix a small number of hydrogel particles near the x-y boundaries to provide anchoring for the elastic deformation of the hydrogel; however, the boundaries are kept sufficiently far away from the biofilm to minimize any boundary effects.

Calculation of the stresses

To quantify stress distribution in our complex system containing active growing/dividing bacteria and passive hydrogels, we define the stress tensor using Virial expression (11), augmented by a contribution from ambient viscosity. The stress tensor is naturally separated in a contribution from interactions and a contribution from environmental viscosity, as $\sigma = \sigma^{int} + \sigma^{vis}$, with

$$\sigma_i^{int} = \frac{1}{V}\Sigma_j r_{ij} \otimes F_{ij}, \tag{18}$$

where F_{ij} is the summation of all particle-particle interactions between particle i and j, and r_{ij} is the distance vector between particle i and j, and V is the cell volume. The viscosity part of Virial stress is given by

$$\sigma_i^{vis} = \frac{1}{V}\Sigma r_i \otimes F_i, \tag{19}$$

where F_i is any viscous force such as the ambient viscous force in Eq. (13) and the substrate viscous force in Eq. (15), r_i is the equivalent acting point of the given viscous force. The summation goes over all types of viscosity, and the definition of σ^{int} and σ^{vis} can be apply to both rod-shaped bacteria and sphere-shaped gel particles. Namely, for the translational ambient viscosity, the contribution to the viscosity stress can be written as $\sigma_i^{vis} = \frac{1}{V}\int_{-L/2}^{L/2} x \otimes (-\eta v)dx$,

where v is the velocity vector of the cell center of mass and x is the relative position vector to the cell center. Similarly, the contribution of rotational ambient viscosity can be given by $\sigma_i^{vis} = \frac{1}{2V}\int_{-L/2}^{L/2} x \otimes (-\omega \times x)dx$, where ω is the angular velocity vector.

Calculation of cell ordering

We use the Q-tensor model of liquid crystals (12) to quantify the local biofilm cell ordering. We calculate the per-cell traceless quantity $Q_i = (3\hat{n}_i \otimes \hat{n}_i - I)/2$, where i denotes the i^{th} cell and I denotes the identity tensor. Compared with the cell director $\hat{n}_i$, Q_i is head-tail symmetric given by $Q_i(\hat{n}_i) = Q_i(-\hat{n}_i)$. Considering the axisymmetric shape of biofilm, we use discretized bins under cylindrical coordinates $\Delta r = 1\mu m$, $\Delta z = 1\mu m$ and $\Delta\theta = \pi/4$ and average Q in each cylindrical bins generating the locally averaged order parameter $Q(r_i,\theta_j,z_k)$, where r_i,θ_j,z_k denotes the bin numbered with (i,j,k). The visualization of the azimuthally averaged Q is calculated by averaging the azimuthally projected order parameter $Q_p = R^T Q R$ over the angle θ. Finally, we take the scalar order parameter S as the maximum eigenvalue of $< Q_p >$ and its eigenvector $\hat{e}$ as the averaged cell director.

Similarly, we define the bipolar order parameter S_b as following. First, we use the coordinates of boundary cells to reconstruct the biofilm-gel interface. Next, for every single outmost cell, we define the local surface normal n_{norm}. Also, we define the position vector r_i by calculating the position of each cell i relative to the biofilm center. The bipolar order parameter S_b is defined as $S_b = 1/2\left(3\left|n_i^{'} \cdot r_i^{'}\right| - 1\right)$, where $n_i^{'}$ and $r_i^{'}$ are the normalized projection vector of n_i and r_i onto the local tangent plane defined by n_{norm}, respectively. S_b is averaged over three outmost layers of cells to reduce randomness.

Biofilm growth dynamics and morphology from ABM

As shown in **Fig. S2**, our model is able to reproduce the growth dynamics of G-II biofilm from the early stage to the mature state: Starting with a single cell lying on the glass surface, cells first

proliferate and form an 2D layer. When the local in-plane pressure accumulates and reaches the threshold for verticalization instability (4), cells tend to be vertical then release part of the growth pressure, and this process generates the initial out-of-plane growth for the transition from 2D expansion to 3D growth of a biofilm. Biofilms deform the surrounding gel during its expansion, resulting different level of growth-induced stress which depends on the biofilm volume and gel stiffness. The stiffness-dependent morphology change is also quantitively captured by our agent-based model. We tune the Young's modulus of surrounding gel from 10^1 to $10^4\,Pa$ and find a sharp transition in biofilm shape around $E_{gel} = 10^2\,Pa$, quantitively reproducing the experimentally observed domes-to-lenses shape transition. More detailed phase diagram of contact angle about Young's modulus of gel and the biofilm-substrate friction can be also found in the reference (13).

G-II biofilm simulations

We have shown the spatiotemporal evolution of hydrostatic pressure, equivalent shear stress, density and rotational speed in the G-I biofilms. Here for completeness and further verification of our hypothesis, the same physical quantities are visualized in **Fig. S5** and **Fig. S6**. As shown in **Fig. S5**, the spatial distribution of stresses shares similar characteristics with the G-I biofilm. Specifically, the pressure and shear stress follow the same trends from the inner region of G-II biofilm to the outer region. Near the center, the pressure is the highest and the equivalent shear stress is relatively low, and near the biofilm-gel interface, the pressure goes down, but the equivalent shear stress reaches its maximum. Since G-II biofilm has same experimental settings except the existence of the rigid glass substrate, the similarity between the pressure and shear stress distribution of G-I and G-II biofilms can be explained by regarding the glass substrate as a plane of symmetry to the first order. However, the existence of the rigid substrate slightly changes the first principal stress direction of the bottom layer of G-II biofilm, from randomly oriented in x-y plane to mostly in z direction, due to cell verticalization (14-16).

Effects of cell stiffness

As a computational exploration for investigating the effects of cell behaviors to the spatiotemporal evolution of cell ordering, we alter the soft-shell cell stiffness E_0 from relatively soft (~100 Pa) to

relatively rigid (~5000 Pa) and keep other simulation setting unchanged. Previous study (17) has shown the cell stiffness is related to the average size of local aligned group. For the G-I biofilm, we define the bipolarly aligned boundary layer using the following method: Based on the reconstructed biofilm-gel interface, we define a series of self-similar ellipsoid surfaces by the interval of long-axis $\Delta L = 0.2\mu m$, as the possible inner surface of the boundary layer. Then we increase the thickness by the increment ΔL and calculate the averaged bipolar order parameter S_b for all cells between the biofilm-gel interface and the given inner surface. The region where $S_b > 0.4$ is regarded as the bipolar boundary layer, and its thickness is defined as the length difference of two long axis of the boundaries. As shown in **Fig. S7**, we indeed observe a two-fold change in the thickness of boundary aligned layer when changing the E_0 from $100\ Pa$ to $5\ kPa$, which can be explained as the increase of energy cost for neighbor cells to have nonparallel configuration and overlap.

Numerical experiments of lateral pressure

As shown in **Fig. 5**, to further illustrate the bidirectional coupling effects between cell ordering and stresses, we design a numerical experiment by imposing an artificial compression on lateral direction. The G-II biofilm is first growing under normal condition (without lateral pressure) for ~10 hrs; then we impose lateral pressure by biaxially deforming the surrounding gel boundary by $\frac{\Delta L_x}{L_x} = 0.2$ and $\frac{\Delta L_y}{L_y} = 0.2$. Denote the time point imposing lateral compression as t_0, we measure the evolution of average shear stress τ_{eq} and the alignment parameter $\alpha = |\hat{n}_1 \cdot \hat{n}_c|$ during the time window $-0.2 < \frac{t - t_0}{T_{double}} < 1$. We find that the lateral compression nearly instantly changes the stress state across the whole biofilm. In contrast, the reorientation process takes roughly $\frac{T_{double}}{2}$ to reach a steady value, indicating the existence of local energy barriers for each cell due to the configuration of neighboring particles.

Numerical experiments with spatially patterned gel stiffness

We design a variation of G-II biofilm simulation by spatially patterning the surrounding gel stiffness. We set the gel modulus 10-fold softer inside a cylindrical region, with the center line pass through the initial seeding cell and the radius of $20\ \mu m$. The remaining part of gel has the homogeneous Young's modulus of $20\ kPa$. Under this confinement settings, we observe significant morphology change and different cell alignment compared with normal simulation of G-II biofilms. Namely, the part of biofilm under the soft region forms a "bleb" indicating non-uniform indentation depth of the soft part of the gel. Also, compared with normal G-II biofilms, significant number of cells are verticalized due to altered first principal stress direction. Our numerical experiments demonstrate the possibility of mechanically controlling biofilm morphology and cell ordering, and it might lead to more precise spatiotemporal control of the stress field and cell orientation field inside the biofilms.

Details of experimental measurements

Bacterial strains and cell culture

The details of bacterial strains can be found in the reference [12]. The biofilm growth experiments begin by first growing *V. cholerae* cells in LB broth (BD) overnight under shaken conditions, then back-diluted 30× in M9 media and grown under shaken conditions until reaching an optical density (OD) of 0.05-0.25. Different concentrations of agarose polymer are boiled in M9 media and then placed in a water bath to cool to 40-50°C without gelation. A 1 μL droplet of the bacterial culture is placed in the center of a glass-bottomed 96 well plate (MatTek) after being diluted in M9 media to an OD of 0.001-0.003. The bacteria are sandwiched between the solidified gel and the glass substrate by the 20 μL of liquid agarose that is used to cover the droplet. (Note that we ignore the droplet's ~5% dilution of the agarose.) In order to serve as a nutrient reservoir, 200 μL of M9 media is put in the well on top of the solidified agarose. Finally, cells are cultivated in static conditions at 30°C and imaged throughout several developmental stages.

Overview of image analysis

Raw images are first deconvolved using Huygens 20.04 (SVI) using a measured point spread function. The deconvolved three-dimensional confocal images are then binarized, layer by layer, with a locally adaptive Otsu method. To accurately segment individual bacterium in the densely packed biofilm, we develop an adaptive thresholding algorithm. Once segmented, we extract the

cell positions by finding the center of mass of each object, and the cell orientations by performing a principal component analysis. The positions and directions of each cell are converted from cartesian $(x,y,z,\hat{n}_x,\hat{n}_y,\hat{n}_z)$ to cylindrical polar $(r,\psi,z,\hat{n}_r,\hat{n}_\psi,\hat{n}_z)$ coordinates where the origin is found by taking the center of mass of all of the segmented cells in the (x,y) plane. Reconstructed biofilm images are rendered using Paraview.

References

1. Beroz, F., Yan, J., Meir, Y., Sabass, B., Stone, H.A., Bassler, B.L. and Wingreen, N.S., 2018. Verticalization of bacterial biofilms. Nature physics, 14(9), pp.954-960.
2. Farrell, F.D.C., Hallatschek, O., Marenduzzo, D. and Waclaw, B., 2013. Mechanically driven growth of quasi-two-dimensional microbial colonies. Physical review letters, 111(16), p.168101.
3. Ghosh, P., Mondal, J., Ben-Jacob, E. and Levine, H., 2015. Mechanically-driven phase separation in a growing bacterial colony. Proceedings of the National Academy of Sciences, 112(17), pp.E2166-E2173.
4. Nijjer, J., Li, C., Zhang, Q., Lu, H., Zhang, S. and Yan, J., 2021. Mechanical forces drive a reorientation cascade leading to biofilm self-patterning. Nature communications, 12(1), p.6632.
5. Yan, J., Nadell, C.D., Stone, H.A., Wingreen, N.S. and Bassler, B.L., 2017. Extracellular-matrix-mediated osmotic pressure drives Vibrio cholerae biofilm expansion and cheater exclusion. Nature communications, 8(1), p.327.
6. Tuson, H.H., Auer, G.K., Renner, L.D., Hasebe, M., Tropini, C., Salick, M., Crone, W.C., Gopinathan, A., Huang, K.C. and Weibel, D.B., 2012. Measuring the stiffness of bacterial cells from growth rates in hydrogels of tunable elasticity. Molecular microbiology, 84(5), pp.874-891.
7. Willis, J.R., 1966. Hertzian contact of anisotropic bodies. Journal of the Mechanics and Physics of Solids, 14(3), pp.163-176.
8. Rentsch S, Pericet-Camara R, Papastavrou G, Borkovec M. Probing the validity of the Derjaguin approximation for heterogeneous colloidal particles. Physical Chemistry Chemical Physics. 2006;8(21):2531-8.
9. Nijjer, J., Li, C., Kothari, M., Henzel, T., Zhang, Q., Tai, J.S.B., Zhou, S., Cohen, T., Zhang, S. and Yan, J., 2023. Biofilms as self-shaping growing nematics. Nature Physics, 19(12), pp.1936-1944.
10. Gusev, A.A., 2004. Finite element mapping for spring network representations of the mechanics of solids. Physical review letters, 93(3), p.034302.
11. Subramaniyan, A.K. and Sun, C.T., 2008. Continuum interpretation of virial stress in molecular simulations. International Journal of Solids and Structures, 45(14-15), pp.4340-4346.
12. Andrienko, D., 2018. Introduction to liquid crystals. Journal of Molecular Liquids, 267, pp.520-541.
13. Nijjer, J., Li, C., Kothari, M., Henzel, T., Zhang, Q., Tai, J.S.B., Zhou, S., Cohen, T., Zhang, S. and Yan, J., 2023. Biofilms as self-shaping growing nematics. Nature Physics, 19(12), pp.1936-1944.
14. Son, K., Guasto, J.S. and Stocker, R., 2013. Bacteria can exploit a flagellar buckling instability to change direction. Nature physics, 9(8), pp.494-498.
15. You, Z., Pearce, D.J., Sengupta, A. and Giomi, L., 2019. Mono-to multilayer transition in growing bacterial colonies. Physical review letters, 123(17), p.178001.
16. Boyer, D., Mather, W., Mondragón-Palomino, O., Orozco-Fuentes, S., Danino, T., Hasty, J. and Tsimring, L.S., 2011. Buckling instability in ordered bacterial colonies. Physical biology, 8(2), p.026008.
17. You, Z., Pearce, D.J., Sengupta, A. and Giomi, L., 2018. Geometry and mechanics of microdomains in growing bacterial colonies. Physical Review X, 8(3), p.031065.

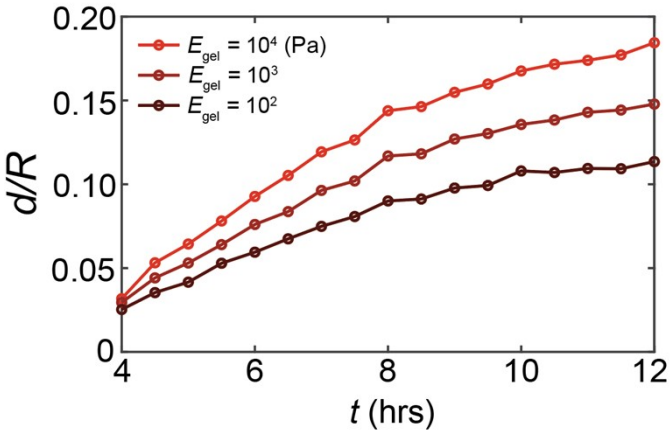

433
434

435 **Fig. S1. Time evolution of the thickness of the boundary layers *d* relative to the biofilm radius**

436 ***R* in the simulated G-I biofilms confined by gels of various stiffnesses.**

437
438

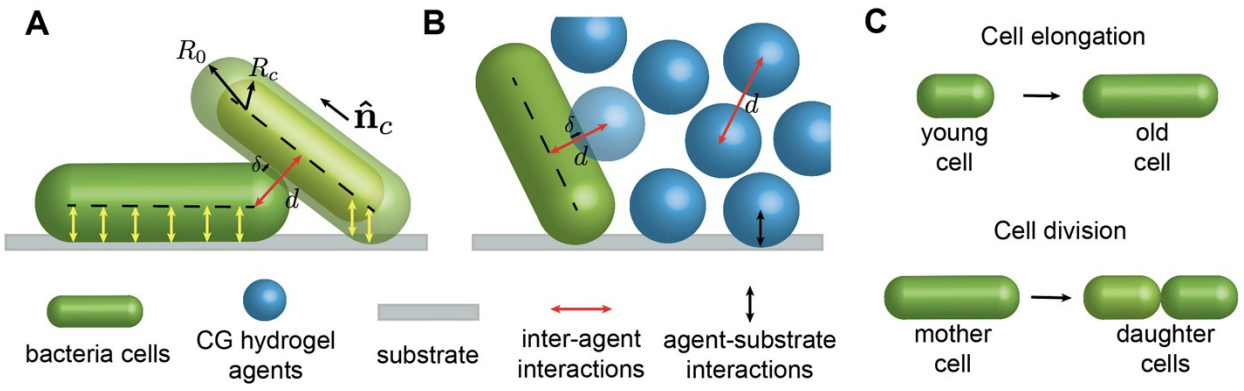

Fig. S2. A schematic illustration of agent-based model. A. Cell-cell interactions. The unit vector $\hat{n}$ represents the director of a single cell. **B.** Cell-gel interactions. **C.** Schematics of cell growth and division. After cell division, the mother cell is replaced by two daughter cells with nearly equal length.

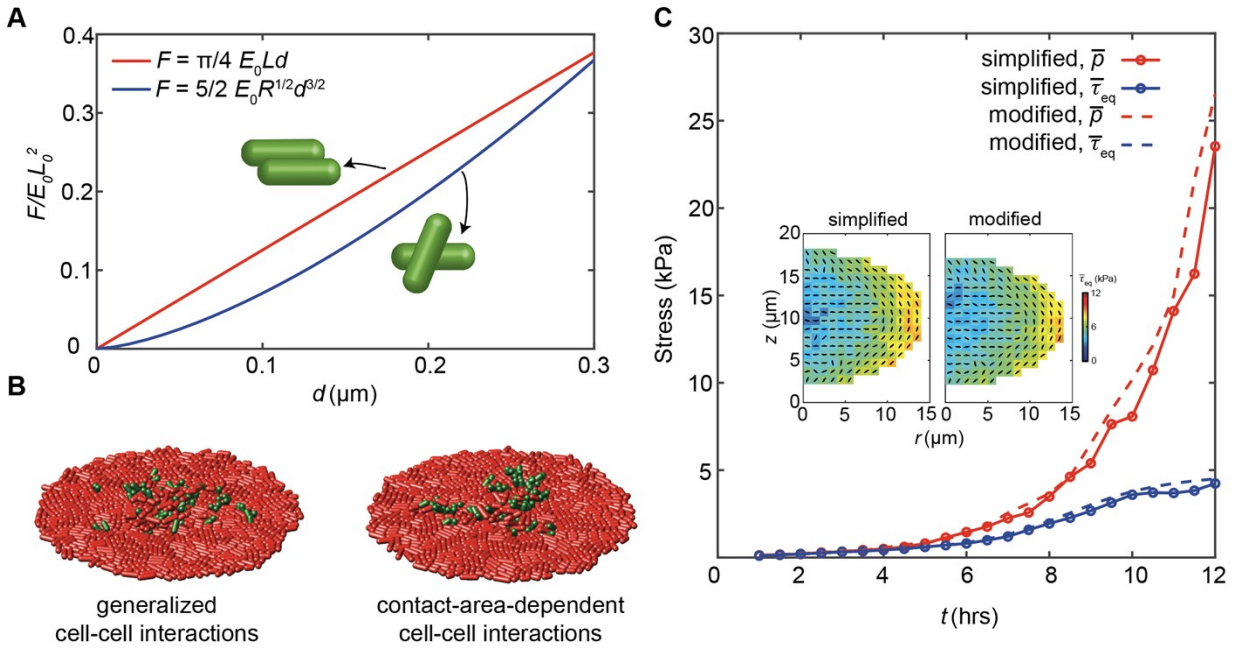

445

446 **Fig. S3. Comparison between different Hertzian contact models. A.** Red solid line: the force-
447 displacement relation of the contact between two parallel cylinders. Blue solid line: the contact
448 between two unparallel cylinders. **B.** The comparison between the generalized contact interaction
449 (left) and the contact-area-dependent interaction. The simplification does not introduce observable
450 error on cell alignment and the onset threshold for cell verticalization. **C.** The comparison of
451 spatiotemporal evolution of hydrostatic pressure and the equivalent shear stress. Inset: the spatial
452 distribution of the equivalent shear stress and the azimuthally averaged cell direction.

453

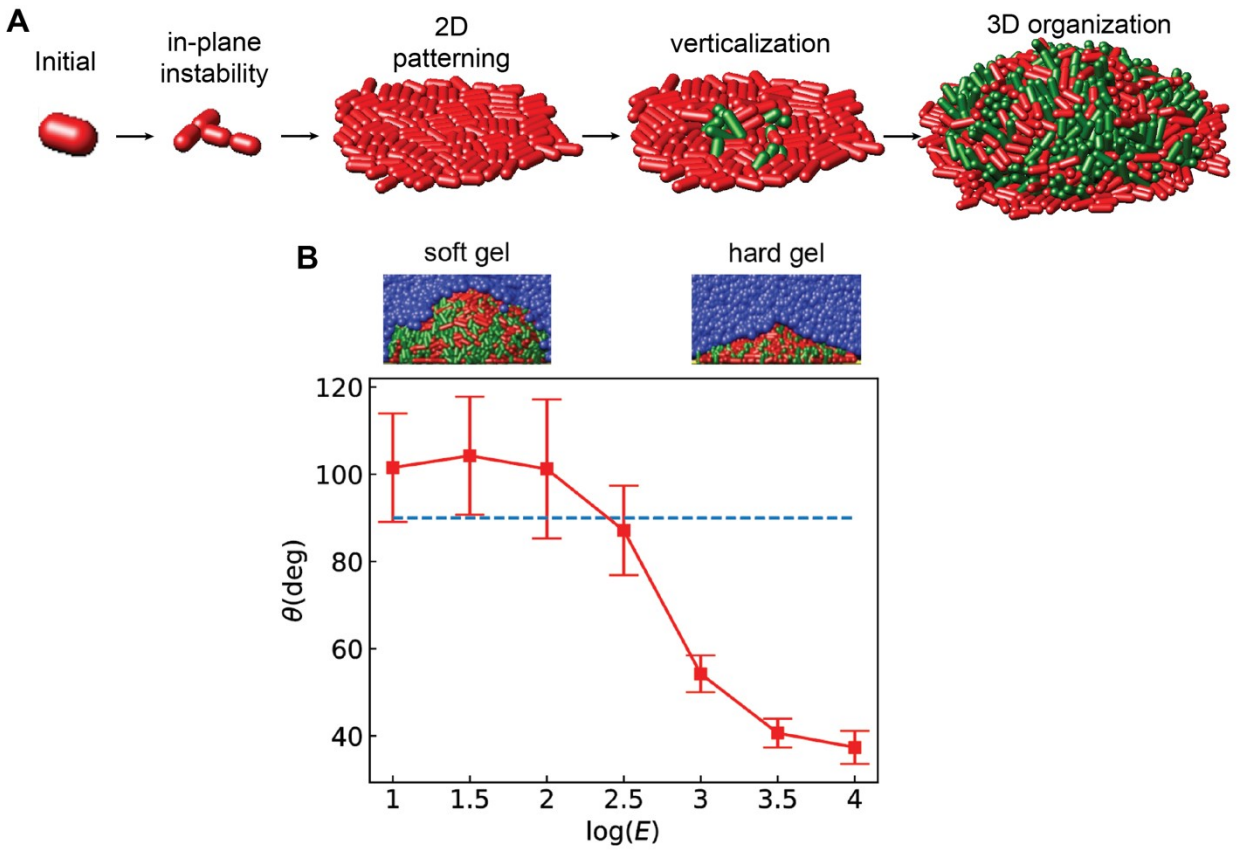

Fig. S3. Agent-based model captures biofilm growth morphodynamics. A. Representative G-II biofilm formation process given by agent-based simulations. **B.** Contact angle changes with the Young's modulus of the surrounding gel. Blue dashed line: 90 degrees. Top subfigures: the cross-section view of the mature (grown after 12 hrs.) G-II biofilm in soft gel (E_{gel}~$10^2\ Pa$) and hard gel (E_{gel}~$10^4\ Pa$).

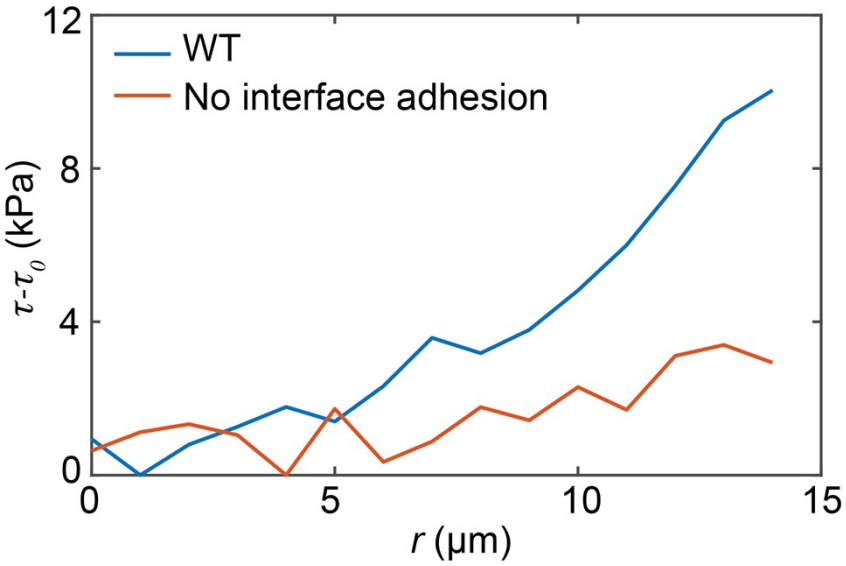

Fig. S4. Transmission of boundary shear stress. Compared with WT biofilm (with normal interface adhesion), biofilms without interface adhesion have significantly less boundary shear stress. The distance r is defined by the long axis length of self-similar ellipsoids.

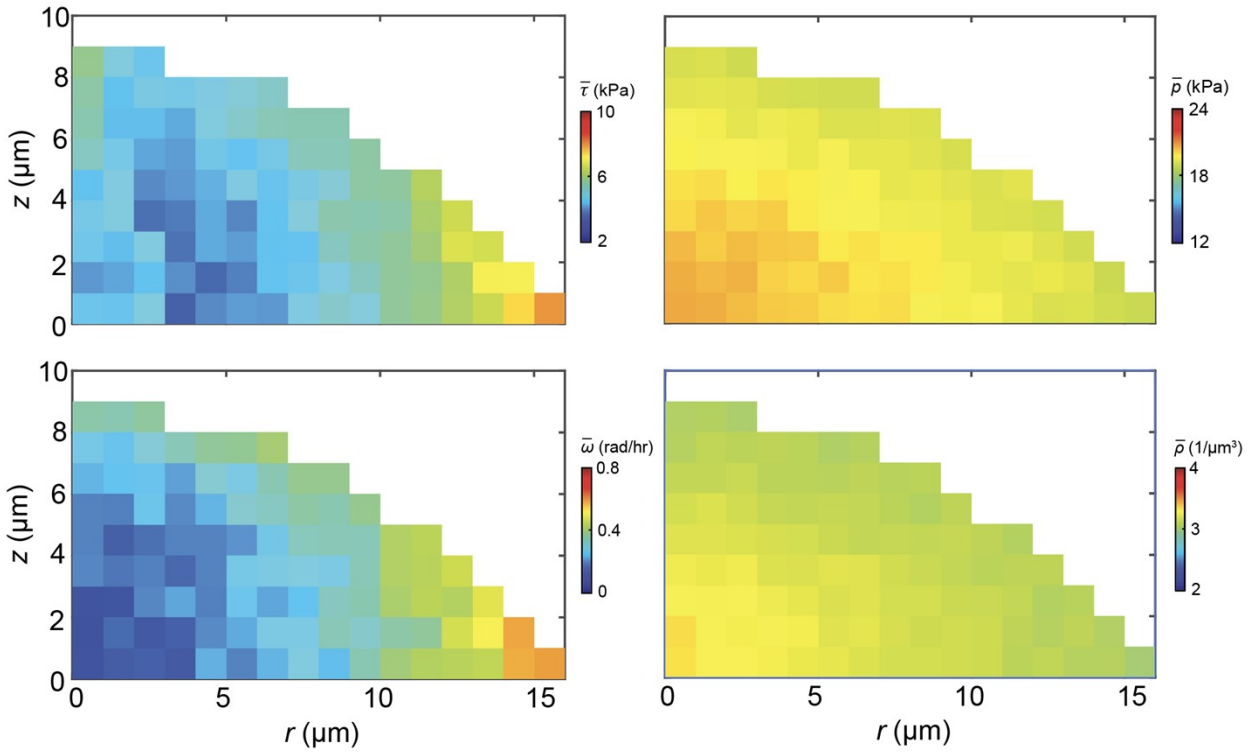

Fig. S5. Spatial distribution of stresses, density and rotation speed of G-II biofilms. A. Spatial distribution of the equivalent shear stress. **B.** Spatial distribution of hydrostatic pressure. **C.** Rotational speed. **D.** Cell density.

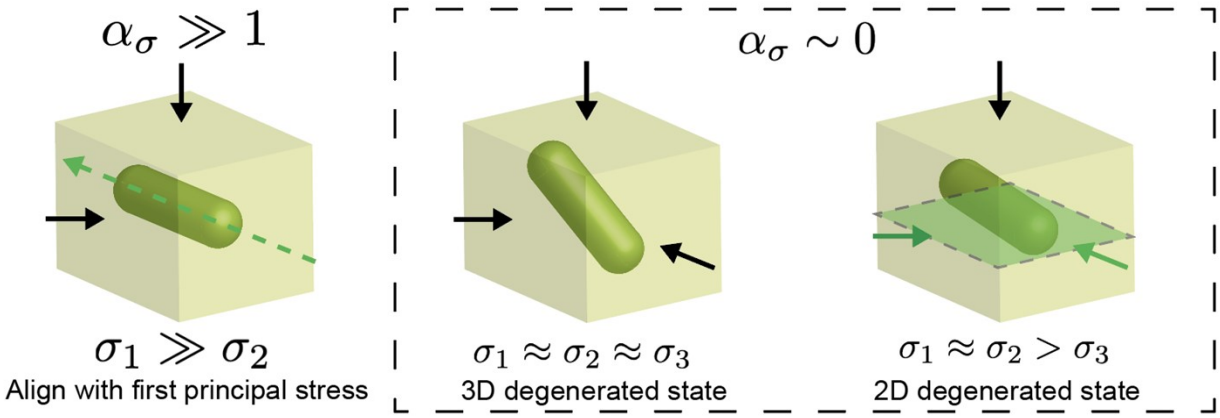

Fig. S6. Schematics illustration of possible stress states in biofilms. Black and green arrows denote the directions of the principal stresses. Green plane with black dashed boundary represents the degenerate plane of minimal compression.

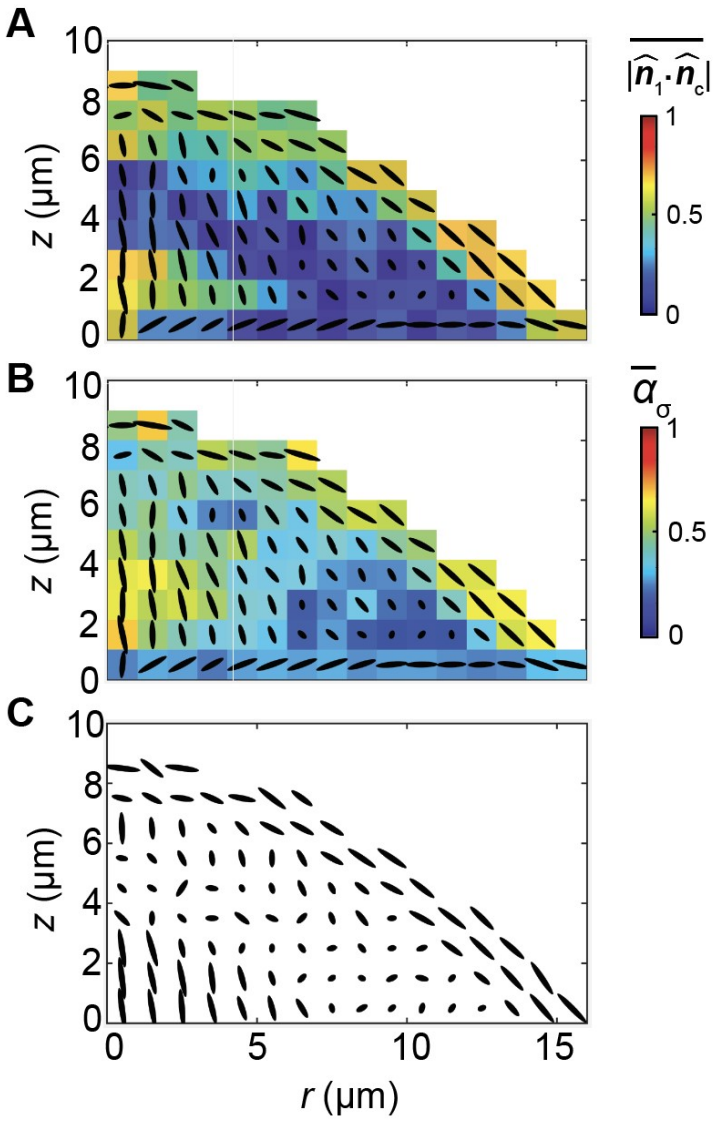

Fig. S7. Spatial distribution of alignment $|\hat{n}_1 \cdot \hat{n}_c|$., stress anisotropy and direction of first principal stress of G-II biofilms. A. Alignment $|\hat{n}_1 \cdot \hat{n}_c|$. **B.** Stress anisotropy α_σ. **C.** Direction of first principal stress.

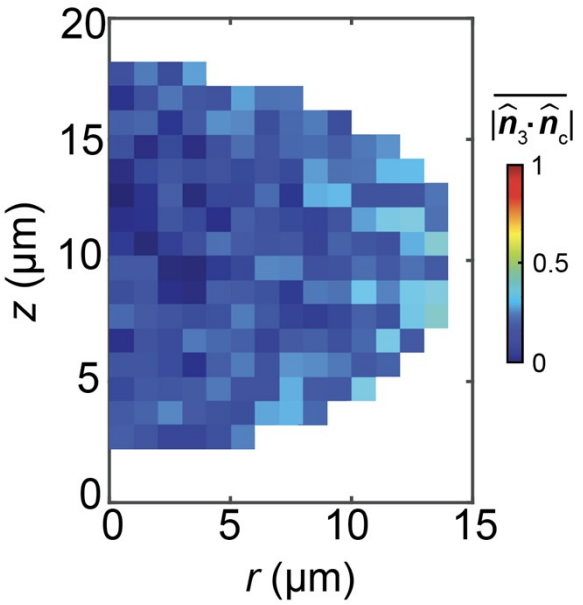

Fig. S8. The spatial distribution of $|\hat{n}_3 \cdot \hat{n}_c|$. Growth time: 10 hours.

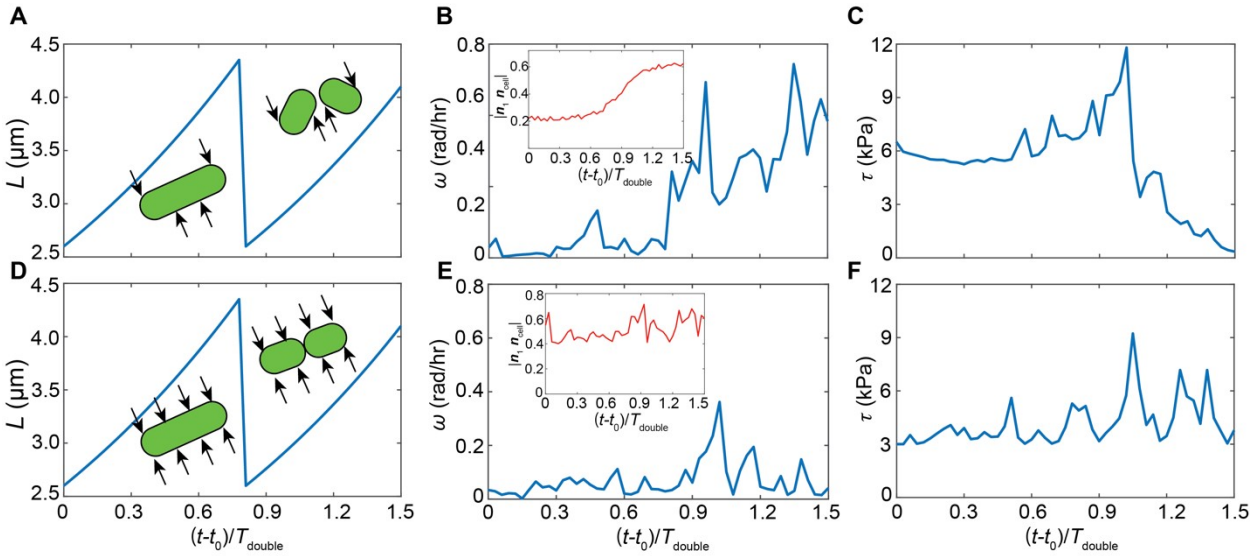

Fig. S9. Representative traces for unstable (A-C) and stable (D-F) configurations of a cell after division. A. Time evolution of single cell length before/after cell division. Inset: Schematic illustration of mechanical instability after cell division. **B.** Time evolution of the cell rotation speed before/after cell division. Inset: Time evolution of alignment $|\hat{n}_1 \cdot \hat{n}_c|$. **C.** Time evolution of the equivalent shear stress. **D-F.** Representative traces of cell length (**D**), rotation speed (**E**) and shear stress (**F**) for a stable configuration after division, respectively.

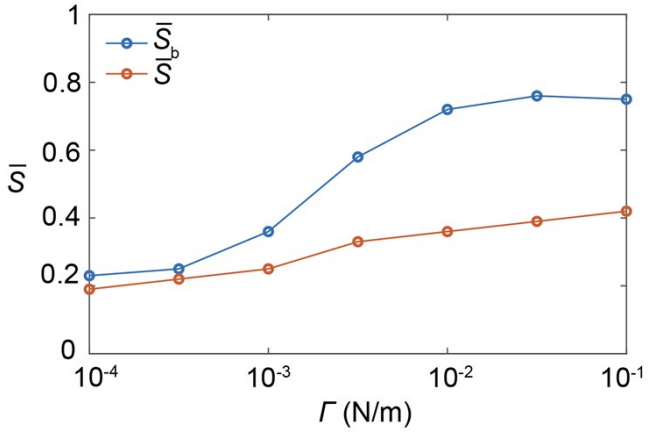

Fig. S10. Biofilm-gel interfacial adhesion controls boundary cell ordering. Blue solid line: The boundary bipolar ordering S_b changes with the interfacial adhesion Γ. Orange solid line: the overall ordering S also has a slight increase with Γ, mainly due to the increase of the boundary ordering.

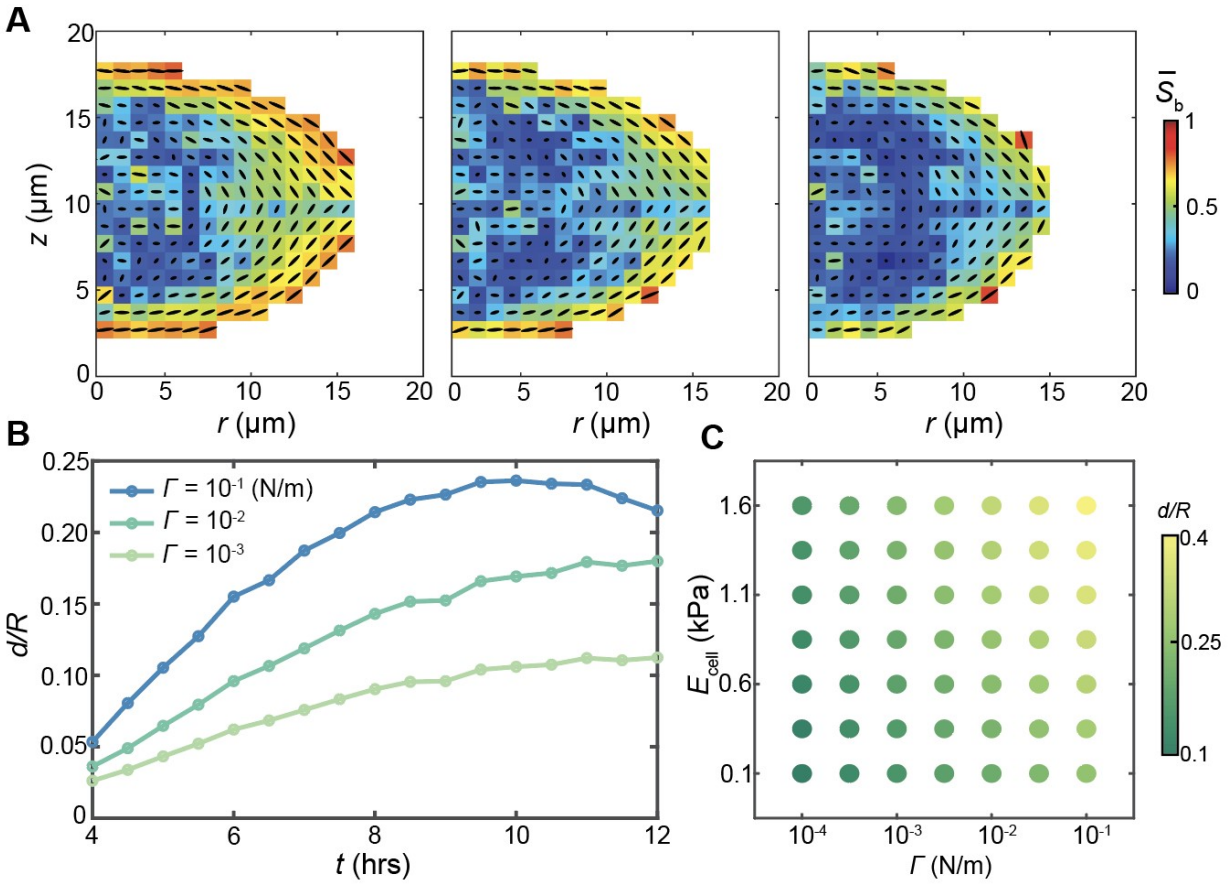

Fig. S11. The effect of cell stiffness and interfacial adhesion on the thickness of boundary layer. (A) Three representative G-I biofilm with different cell-gel adhesion, hence different thicknesses of boundary alignment layer. **(B)** Time evolution of boundary layer thickness for various cell-gel adhesion Γ. **(C)** Phase diagram showing the relation between boundary layer thickness d, cell stiffness E_{cell}, and cell-gel adhesion Γ.